Chapter 4

The Role of Volcanic Activity in Climate and Global Change

Georgiy Stenchikov
Department of Environmental Sciences, Rutgers University, New Brunswick, New Jersey 08901-855

1. INTRODUCTION

Volcanic activity is an important natural cause of climate variations because tracer constituents of volcanic origin impact the atmospheric chemical composition and optical properties. This study focuses on the recent period of the Earth's history and does not consider a cumulative effect of the ancient volcanic degassing that formed the core of the Earth's atmosphere billions of years ago. At present, a weak volcanic activity results in gas and particle effusions in the troposphere (lower part of atmosphere), which constitute, on an average, the larger portion of volcanic mass flux into the atmosphere. However, the products of tropospheric volcanic emissions are short-lived and contribute only moderately to the emissions from large anthropogenic and natural tropospheric sources. This study focuses instead on the effects on climate of the Earth's explosive volcanism. Strong volcanic eruptions with a volcanic explosivity index (VEI) [1] equal to or greater than 4 could inject volcanic ash and sulfur-rich gases into the clean lower stratosphere at an altitude about 25–30 km, increasing their concentration thereby two to three orders of magnitude in

Climate Change: Observed Impacts on Planet Earth

comparison with the background level. Chemical transformations and gas-to-particle conversion of volcanic tracers form a volcanic aerosol layer that remains in the stratosphere for 2–3 years after an eruption, thereby impacting the Earth's climate because volcanic aerosols cool the surface and the troposphere by reflecting solar radiation, and warm the lower stratosphere, absorbing thermal IR and solar near-IR radiation [2]. Figure 1 shows stratospheric optical depth for the visible wavelength of 0.55 μm. It roughly characterises the portion of scattered solar light. Three major explosive eruptions occurred in the second part of the twentieth century, as depicted in Fig. 1: Agung of 1963, El Chichon of 1982, and Pinatubo of 1991.

Volcanic eruptions, like the Mt. Pinatubo eruption in 1991, with global visible optical depth maximizing at about 0.15, cause perturbation of the globally averaged radiative balance at the top of the atmosphere reaching -3 W·m^{-2} and cause a decrease of global surface air temperature by 0.5 K. Radiative impact of volcanic aerosols also produces changes in atmospheric circulation, forcing a positive phase of the Arctic Oscillation (AO) and counterintuitive

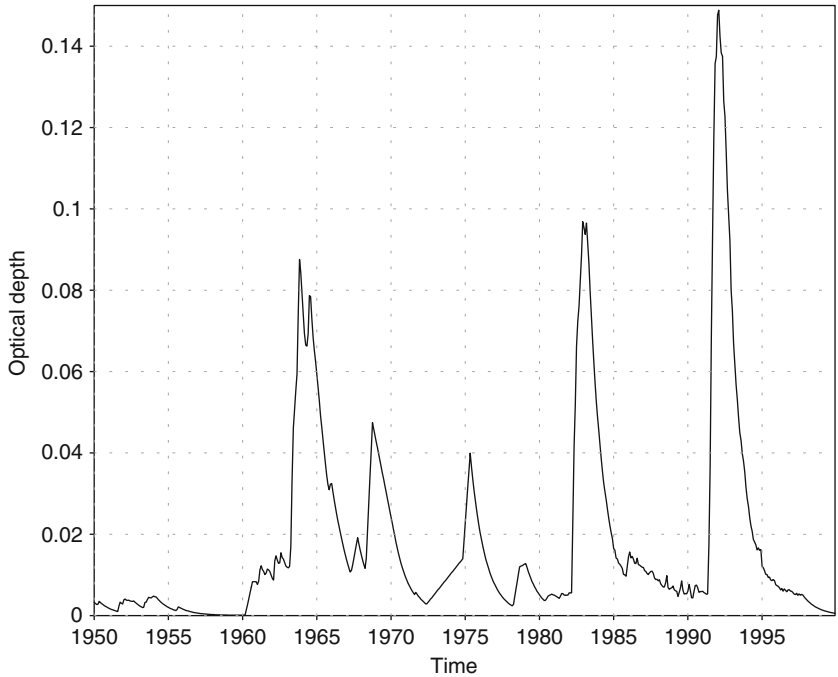

FIGURE 1 The total global mean normal optical depth τ of stratospheric aerosols for the Pinatubo period for the visible wavelength of 0.55 μm as a function of time. It causes attenuation of direct solar visible light with a factor of $\exp(-\tau/\cos\zeta)$, where $\cos\zeta$ is a cosine of zenith angle.

boreal winter warming in middle and high latitudes over Eurasia and North America [3–8]. In addition, stratospheric aerosols affect stratospheric chemistry serving as surfaces for heterogeneous reactions liberating anthropogenic chlorine and causing ozone depletion.

It was traditionally believed that volcanic impacts produced mainly short-term transient climate perturbations. However, the ocean integrates volcanic radiative cooling, and different components of the ocean respond over a wide range of time scales. Volcanically induced tropospheric temperature anomalies vanish in about 7 years, while volcanically induced sea ice extent and volume changes have a relaxation time scale closer to a decade. Volcanically induced changes in interior ocean temperature, the meridional overturning circulation (MOC), and steric height, have even longer relaxation times, from several decades to a century. Because of their various impacts on climate systems, volcanic eruptions play a role of natural tests, providing an independent means of assessing multiple climate feedback mechanisms and climate sensitivity [7–11].

There are several excellent reviews devoted to volcanic impacts on climate and weather [12–19]. The present study provides an overview of available observations of volcanic aerosols and discusses their radiative forcing and large-scale effects on climate. It focuses on recently discovered forced stratosphere–troposphere dynamic interaction and long-term ocean response to volcanic forcing, and aims to add information to that already presented in the previous reviews.

2. AEROSOL LOADING, SPATIAL DISTRIBUTION AND RADIATIVE EFFECT

Volcanic emissions comprised of gases (H_2O, CO_2, N_2, SO_2, H_2S) and solid (mostly silicate) particles, that are usually referred to as volcanic ash. Volcanic ash particles are relatively large, exceeding 2 μm in diameter, and therefore deposit relatively quickly, that is, within a few weeks. They are responsible for short-term regional-to-continental perturbations of the Earth's radiative balance and meteorological parameters. H_2O, CO_2 and N_2 are abundant in the Earth's atmosphere, so individual volcanic perturbations of their concentrations are negligible. But SO_2 and H_2S, which quickly oxidize to SO_2 if erupted in the stratosphere, could significantly affect stratospheric chemical composition and optical properties. SO_2 gas absorbs UV and IR radiation, producing very strong localized stratospheric heating [20–22]. However, it completely disappears in about half a year and the major long-term impact of volcanic eruptions on climate is due to long-lived sulfate aerosols formed by oxidizing of SO_2 with a characteristic conversion time of about 35 days. Sulfate volcanic aerosols (submicron droplets of highly concentrated sulfuric acid) are transported globally by the Brewer–Dobson stratospheric circulation

and eventually fall out in 2–3 years. A significant amount of volcanic aerosols that penetrate to the troposphere through the tropause folds is washed out in storm tracks. Aerosols deposited in downward branches of the Brewer–Dobson circulation in the Polar Regions are preserved in the polar ice sheets, recording the history of the Earth's explosive volcanism for thousands of years [23–25]. However, the atmospheric loadings calculated using volcanic time series from high-latitude ice records, suffer from uncertainties in observation data and poor understanding of atmospheric transport and deposition processes. The global instrumental observations of volcanic aerosols have been conducted during the last 25 a (years) by a number of remote sensing platforms. Total Ozone Mapping Spectrometer (TOMS) instrumentation onboard the Nimbus-7 provided SO_2 loadings from November 1978 until 6 May 1993 [26]. Prata et al. [27] recently developed a new retrieval technique to obtain SO_2 loadings from TOMS data. The Advanced Very High Resolution Radiometer (AVHRR) provides aerosol optical depth over oceans with 1 km spatial resolution in several visible and near-IR wavebands. However, column observations are not sufficient to reliably separate tropospheric and stratospheric aerosols.

The Stratospheric Aerosol and Gas Experiment (SAGE) and Stratospheric Aerosol Measurement (SAM) projects have provided more than 20 a of vertically resolved stratospheric aerosol spectral extinction, the longest such record. The 3-D observations are most valuable to understand stratospheric aerosols transformations and transport. However, there are significant gaps in the temporal-spatial coverage, for example, the eruption of El Chichón in 1982 (the second most important in the twentieth century after Mt. Pinatubo) is not covered by SAGE observations because the SAGE I instrument failed in 1981, and SAGE II was only launched in 1984. Fortunately, instruments aboard the Stratosphere Mesosphere Explorer (SME) filled the gap of 1982–1984 in 3-D aerosol observations. The saturation periods when the SAGE instrument could not see the direct sun light through the dense areas of aerosol cloud also could be partially reconstructed using lidar and mission observations [28,29]. It is important to utilize observations from the multiple platforms to improve data coverage, for example, combining SAGE II and Polar Ozone and Aerosol Measurement (POAM) data could help to fill in the polar regions. Randall et al. [30,31] have extensively intercompared the POAM and SAGE data and normalized them, combining them into a consistent data set.

Cryogenic Limb Array Etalon Spectrometer (CLAES), Improved Stratospheric and Mesospheric Sounder (ISAMS) and Halogen Occultation Experiment (HALOE) instruments launched on the Upper Atmosphere Research Satellite (UARS) provide additional information for the post-Pinatubo period. These instruments measure the aerosol volume extinction (HALOE) and volume emission (CLAES, ISAMS) in the near IR and IR bands. These three

infrared instruments provide better horizontal coverage than SAGE, but do not penetrate lower than the 100 hPa level. They started operating in September 1991. CLAES and ISAMS stopped working after 20 months. The SAGE III instrument aboard the Russian Meteor III-3M satellite continued the outstanding SAGE aerosol data record [32,33] from 2001 to 2007. The new Moderate Resolution Imaging Spectroradiometer (MODIS) and Multiangle Imaging SpectroRadiometer (MISR) instruments have superior spatial and spectral resolutions, but mostly focus on the tropospheric aerosols and surface characteristics, providing column average observations.

Available satellite and ground-based observations were used to construct volcanic aerosol spatial-temporal distribution and optical properties [2,34–39]. Hansen et al. [37] improved a Goddard Institute for Space Studies (GISS) volcanic aerosols data set for 1850–1999, providing zonal mean vertically resolved aerosol optical depth for visible wavelength and column average effective radii. Amman et al. [34] developed a similar data set of total aerosol optical depth based on evaluated atmospheric loadings distributed employing a seasonally varying diffusion-type parameterisation that could also be used for paleoclimate applications (if aerosol loadings are available). Amman et al. [34], however, used a fixed effective radius of 0.42 μm for calculating aerosol optical properties and, in general, provided higher values of optical depth than in Hansen et al. [37]. Stenchikov et al. [39] used UARS observations to modified effective radii from Hansen et al. [37] implementing its variations with altitude, especially at the top of the aerosol layer where particles became very small. They conducted Mie calculations for the entire period since 1850 and implemented these aerosol characteristics in the new Geophysical Fluid Dynamics Laboratory (GFDL) climate model. The sensitivity calculations with different effective radii show that total optical depth vary as much as 20% when effective radius changes are in the reasonable range. The study of Bauman et al. [35,36] provides a new approach for calculating aerosol optical characteristics using SAGE and UARS data. Bingen et al. [40,41] have calculated stratospheric aerosols size distribution parameters using SAGE II data. A new partly reconstructed and partly hypothesized climate forcing time series for 500 years, that includes greenhouse gas (GHG) and volcanic effects, was developed by Robertson et al. [42].

Aerosol optical properties include aerosol optical depth (see Fig. 1), single scattering albedo (to characterize aerosol absorptivity) and asymmetry parameter (to define the directionality of scattering). Using these aerosol radiative characteristics one can evaluate aerosol radiative effect on climate system – aerosol radiative forcing at the top of the atmosphere. Figure 2 shows the total forcing and its short wave (SW) and long wave (LW) components. Increase of reflected SW radiation ranges from 3 to 5 $W \cdot m^{-2}$ but is compensated by aerosol absorption of outgoing LW radiation, so total maximum cooling of the system ranges from 2 to 3 $W \cdot m^{-2}$.

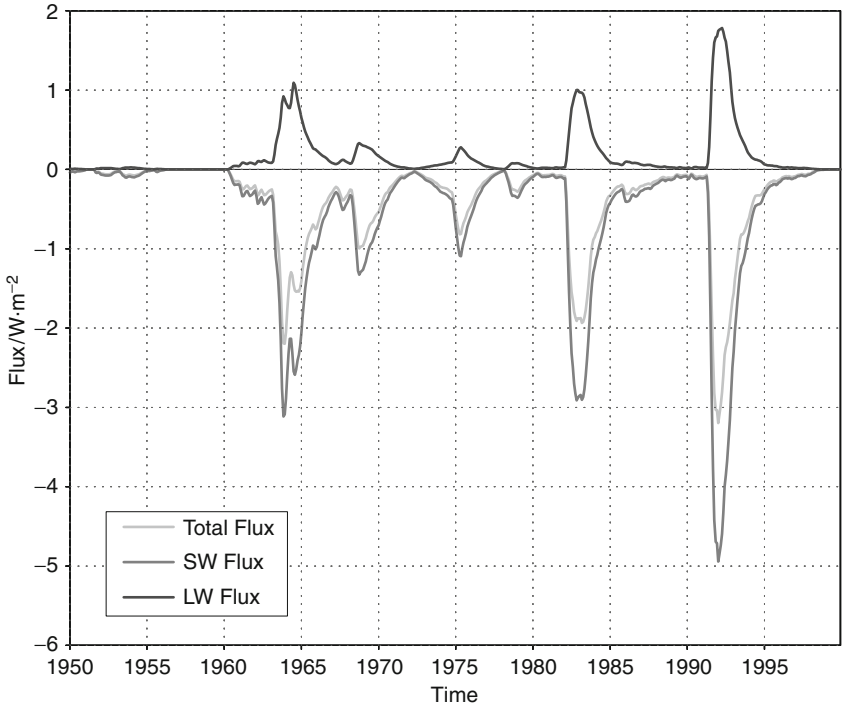

FIGURE 2 Volcanic aerosol total, short wave (SW) and long wave (LW) radiative forcing (W·m^{-2}) at the top of the atmosphere for All-Sky conditions. Positive sign of the forcing corresponds to heating of climate system.

3. VOLCANOES AND CLIMATE

The perturbations of the Earth's radiative balance caused by strong volcanic eruptions dominate other forcings for 2–3 years. Their effect is seen in the atmosphere for about 5–7 years, and, as was recently discovered, for much longer in oceans [43–47]. Volcanic perturbations have been used for years as natural experiments to test models and to study climate sensitivity and feedback mechanisms. Many of these studies have focused on simulating the aftermath of the Mt. Pinatubo eruption in the Philippines at 15.1°N, 120.4°E in June 1991, which was both the largest eruption of the twentieth century and the eruption for which the stratospheric aerosol has been best observed [48–54]. During this eruption about 17 Tg (1 Tg = 10^{12} g) of SO_2 were injected into the lower stratosphere and subsequently converted into sulfate aerosols. There are three main foci of such studies addressed in the present study: analysis of the simulation of atmospheric temperature and precipitation response; simulation of the response of the extratropical circulation in the NH winter to season; and, recently emerged, analysis of volcanic impact on ocean.

The use of volcanic simulations as tests of model climate feedback and sensitivity is somewhat hampered by weather and climate fluctuations because any climate anomalies observed in the aftermath of these eruptions will also reflect other internally generated variability in the atmosphere–ocean system (e.g., El Niño/Southern Oscillation (ENSO), quasi-biennial oscillation (QBO) or chaotic weather changes). Due to limited observations one has to use models to better understand the physical processes forced in the climate system by volcanic impacts. With model simulations, one can perform multiple realizations to clearly isolate the volcanic climate signal, but the real world data are limited to the single realization during the period since quasi-global instrumental records have been available.

Models of different complexity were traditionally used to analyse volcanic climate impacts. Those models might simplify description of atmospheric and/or ocean processes [55], or mimic radiative effect of volcanic aerosol by decreasing of solar constant [56]. In the present study, to illustrate mechanisms of volcanic impacts on climate, a comprehensive coupled climate model, CM2.1, is used. Developed at the National Oceanic and Atmospheric Administration's (NOAA) Geophysical Fluid Dynamic Laboratory (GFDL), CM2.1 was used in the IPCC AR4 study [44,57]. This model calculates both atmosphere and ocean, and accounts interactively for volcanic aerosol radiative forcing. It is composed of four component models: atmosphere, land, sea ice and ocean. The coupling between the component models occurs at 2-h intervals. The atmospheric model has a grid spacing of 2.5° longitude by 2° latitude and 24 vertical levels. The dynamical core is based on the finite volume scheme of Lin [58]. The model contains a completely updated suite of model physics compared to the previous GFDL climate model, including new cloud prediction and boundary layer schemes, and diurnally varying solar insolation. The radiation code allows for explicit treatment of numerous radiatively important trace gases (including tropospheric and stratospheric ozone, halocarbons, etc.), a variety of natural and anthropogenic aerosols (including black carbon, organic carbon, tropospheric sulfate aerosols and volcanic aerosols), and dust particles. Aerosols in the model do not interact with the cloud scheme, so that indirect aerosol effects on climate are not considered. The land model is described in Milly and Shmakin [59]. Surface water is routed instantaneously to ocean destination points on the basis of specified drainage basins. The land cover type in the model uses a classification scheme with 10 different land cover types. The ocean model [60,61] has a nominal grid spacing of 1° in latitude and longitude, with meridional grid spacing decreasing in the tropics to 1/3° near the equator, and uses a tripolar grid to avoid polar filtering over the Arctic. The model has 50 vertical levels, including 22 levels with 10 m thickness each in the top 220 m. A novel aspect is the use of a true fresh-water-flux boundary condition. The sea ice model is a dynamical model with three vertical layers and five ice thickness categories. It uses the elastic-viscous-plastic rheology to calculate ice internal stresses,

and a modified Semtner three-layer scheme for thermodynamics [62]. The aerosol optical characteristics were calculated following Stenchikov et al. [2] using optical depth from Sato et al. [38] and Hansen et al. [37]. The aerosol size distribution was assumed log-normal with fixed width of 1.8 μm [39].

In this study, various volcanic impacts on climate are illustrated using results from the model experiments and available observations. In each case, twin ensembles of volcano and control runs are conducted, and the response of the climate system calculated to volcanic forcing as the ensemble mean over the volcano runs minus the ensemble mean over the control runs. The variability within ensembles is used to estimate the statistical significance of climate signals.

3.1. Tropospheric Cooling and Stratospheric Warming

The analysis for the Pinatubo case is easier than for other big eruptions because aerosols were well observed and the climate responses were relatively well documented. However, Pinatubo erupted in an *El Niño* year and both volcanic and sea surface temperature (SST) effects overlapped at least in the troposphere. ENSO events that occurred near the times of volcanic eruptions could either mask or enhance the volcanic signal. Adams et al. [63] even argued that changing atmospheric circulation caused by volcanic eruptions could cause El Nino. Santer et al. [64] conducted a comprehensive analysis of the ENSO effect on the modelled and observed global temperature trends. Shindell et al. [4] addressed the issue of interfering volcanic and ENSO signals by specific sampling of eruptions so as SST signal will average out in the composite. Yang and Schlesinger [65,66] used Singular Value Decomposition (SVD) analysis to separate spatial patterns of the ENSO and volcanic signals in the model simulations and observations. They showed that ENSO signal is relatively weak over Eurasia but strong over North America contributing about 50% of the responses after the 1991 Mt. Pinatubo eruption.

The ENSO variability issue is addressed in the present study by comparing simulated and observed responses after extracting the *El Niño* contribution from the tropospheric temperature. Santer et al. [64] developed an iterative regression procedure to separate a volcanic effect from an *El Niño* signal using Microwave Sounding Unit (MSU) brightness temperature observations from the lower tropospheric channel 2LT [67]. The globally averaged synthetic 2LT temperature for the Pinatubo ensemble runs is calculated using model output and compared with the response from Santer et al. [64]. The simulated anomaly is calculated with respect to the mean over the corresponding control segments that have the same developing *El Niños* as in the perturbed runs. It is probably an ideal way to remove the *El Niño* effect from the simulations because the exact *El Niño* signal which would have developed in the model if the volcanic eruption did not occur is subtracted. This procedure, however, only works well for the initial *El Niño* when perturbed runs 'remember' their oceanic initial conditions. Figure 3 shows a comparison of synthetic ENSO-subtracted anomaly with the observed

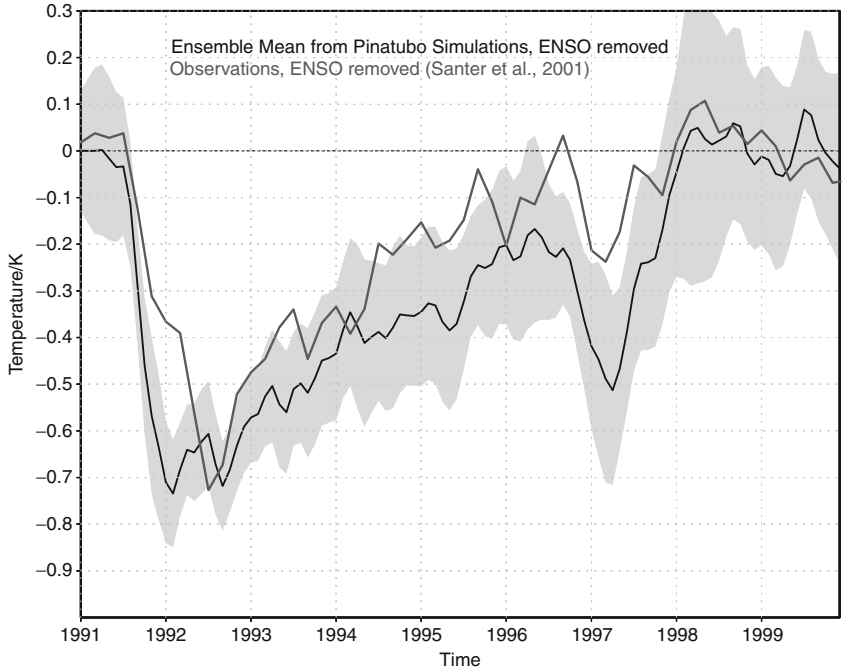

FIGURE 3 The observed Lower Tropospheric MSU 2LT temperature anomaly (K) caused by the Pinatubo eruption from Santer et al. [64] with ENSO effect removed, and the simulated synthetic 2LT ensemble mean temperature anomaly (K) calculated from the Pinatubo ensemble with the *El Niño* 1991 effect removed; shading shows $\pm 2\sigma$ ensemble mean variability.

anomaly from Santer et al. [64] with ENSO removed statistically. Shading shows doubled standard deviation variability for the 10-member ensemble mean. The observed MSU 2LT anomaly itself has much higher variability (not shown) because there is only one natural realization. Thus, the simulated Pinatubo signal in the lower tropospheric temperature reaches −0.7 K; it is statistically significant at 99% confidence level and the difference between simulated and observed responses is below the variability range. The lower tropospheric temperature anomaly reduces below the noise level in about 7 years, which corresponds approximately to the thermal response time of the ocean mixed layer [68].

For the lower stratosphere, a similar comparison was conducted as for the lower troposphere, but without removing ENSO because its effect in the lower stratosphere is fairly small. However, the stratospheric response to volcanic forcing might be affected by the phase of a QBO [7,69]. Figure 4 compares the simulated synthetic MSU channel 4 temperature for the lower stratosphere with the MSU 4 observations. The stratospheric warming is produced by aerosol IR and near-IR absorption. Ramaswamy et al. [70] discussed that the MSU

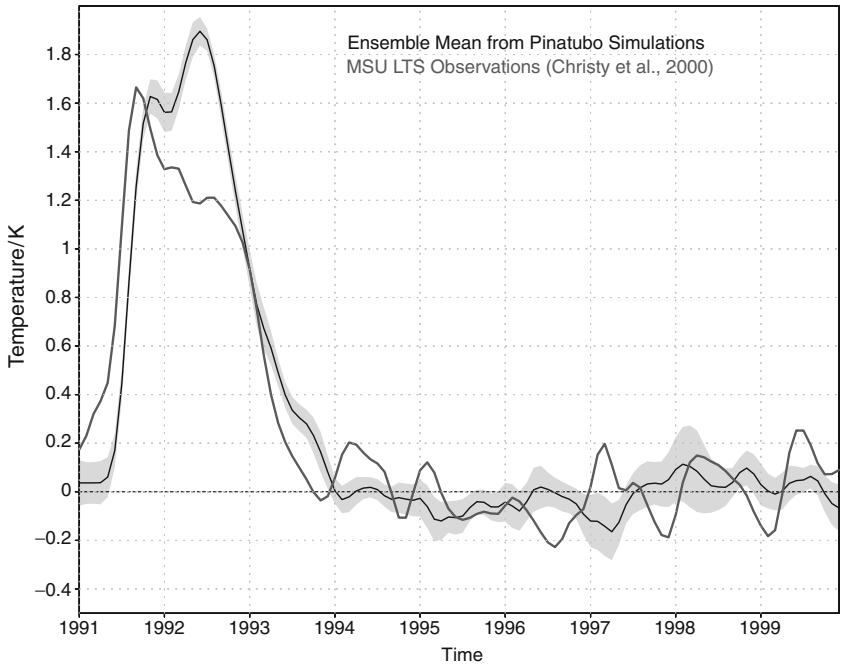

FIGURE 4 The observed MSU 4 Lower Stratospheric temperature anomaly (K) caused by the Pinatubo eruption, and the simulated synthetic channel 4 ensemble mean temperature anomaly (K) calculated from the Pinatubo ensemble; shading shows $\pm 2\sigma$ ensemble mean variability.

lower stratospheric temperature tends to level in a few years after the Pinatubo eruption; therefore, we calculate the anomalies in Fig. 4 with respect to the 1994–1999 mean both in the model and in the observation. The yellow shading shows the $\pm 2\sigma$ ensemble mean variability. The simulated signal compares well with the observation albeit slightly overestimates the stratospheric warming in the second year after the eruption. In the real world, the observed signal could be offset by the easterly phase of QBO in 1992/1993 but not in the model, which lacks QBO. The atmospheric response in the lower stratosphere follows the volcanic forcing and disappears in 3 years, as expected, when volcanic radiative forcing vanishes.

3.2. Effect on Hydrological Cycle

Precipitation is more sensitive to variations of Solar SW Radiation than Thermal IR Radiation because SW radiation directly affects the surface energy budget and links to global precipitation changes through evaporation. Therefore, one could expect that volcanic aerosols might decrease global

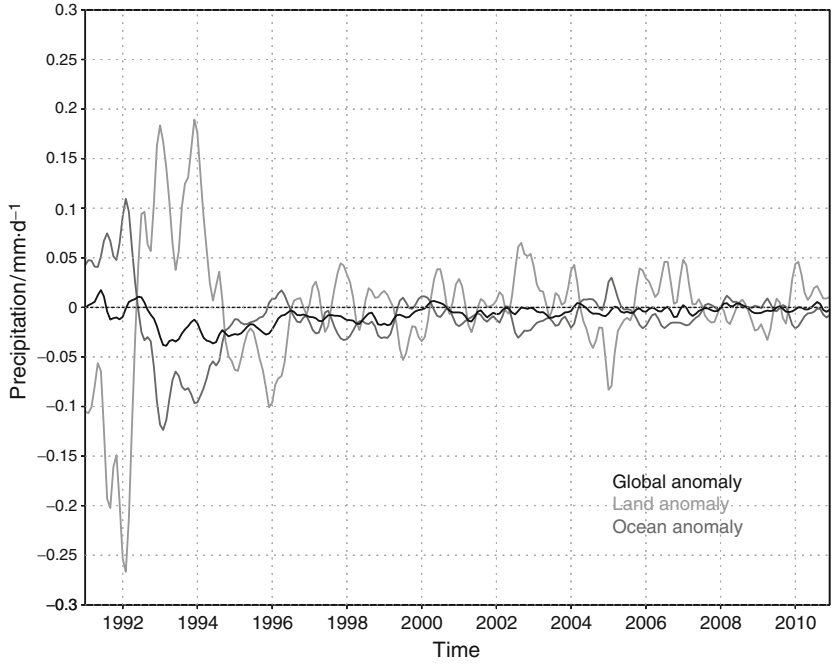

FIGURE 5 Time evolution of ensemble mean precipitation anomaly ($mm \cdot d^{-1}$) caused by Pinatubo eruption averaged over ocean, land, and globally, calculated with respect to a climatological mean.

precipitation for the period of 2–3 years when volcanic SW radiative forcing remains significant. This effect was detected in observations [71] and in model simulations [72,73]. The Pinatubo case-study analysis shows that in the ensemble mean results the global precipitation anomalies (Fig. 5) could be seen for almost 5–6 years because ocean cools and SST relaxes for about 7 years and affects the global hydrologic cycle. The precipitation anomalies over land and over ocean have different dynamics. The land precipitation drops during the first year because of rapid land radiative cooling. The ocean cooling and decrease of precipitation over ocean are delayed and reach maximum values in 3–4 years after the eruption when the sea surface temperature is coldest. The cold SST tends to shift precipitation over land and the land precipitation goes up compensating in part the decrease of precipitation over ocean. Geographically the precipitation anomalies are located in low latitude monsoon regions and could cause significant disruptions of food production in those regions with very high population density. It must be emphasized that ENSO contributes significantly to the observed precipitation anomalies. When ENSO signal is removed in the model results the amplitude of the precipitation anomalies significantly decreases although temporal behaviour does

not change qualitatively. This suggests that in data analysis similar to that conducted by Trenberth and Dai [71], it is important to evaluate and filter out the ENSO contribution.

3.3. Volcanic Effect on Atmospheric Circulation

In the 2 years following major eruptions, the NH winter tropospheric circulation has typically been observed to display features characteristic of an anomalously positive AO index situation. This has a zonal-mean expression with low-pressure at high latitudes and a ring of anomalously high pressure in the mid-latitudes. This basic zonal-mean pattern is modulated by a very strong regional structure with an intensified high pressure anomaly over the North Atlantic and Mediterranean sectors called North Atlantic Oscillation (NAO). Consistent with this are pole-ward shifts in the Atlantic storm track and an increased flow of warm air to Northern Europe and Asia, where anomalously high winter surface temperatures are observed [7,8,39]. It seems that only low-latitude volcanic eruptions could affect the AO/NAO phase and the AO/NAO remain fairly insensitive to the high-latitude NH eruptions [74].

The mechanisms that govern the climate response to volcanic impacts very likely play an important role in global climate change [4,39,75]. The northern polar circulation modes (NAO/AO) experienced significant climate variations during the recent two decades and also are sensitive to volcanic forcing. The southern annular mode (SAM similar to AO) shows recently a very significant climate trend but is not sensitive to volcanic forcing [76]. Supposedly dynamics of the annular mode in the Southern Hemisphere are different than in the Northern Hemisphere and, to a great extent, are controlled by ocean processes and stratospheric ozone variations. In the present study, discussion is limited to NAO/AO.

The most robust effect on atmospheric temperature produced by volcanic aerosols is in the lower stratosphere. It is known that low-latitude explosive eruptions produce anomalously warm tropical lower stratospheric conditions and, in the NH winter, an anomalously cold and intense polar vortex. The tropical temperature anomalies at 50 hPa (Fig. 6) are a direct response to the enhanced absorption of terrestrial IR and solar near-IR radiation by the aerosols. The high-latitude winter perturbations at 50 hPa are a dynamical response to the strengthening of the polar vortex or polar night jet. This is due to stronger thermal wind produced by increasing of the equator-to-pole temperature gradient in the lower stratosphere [6,69,77–81].

The strengthening of the polar jet is amplified by a positive feedback between the polar NH winter vortex and vertical propagation of planetary waves. The stronger vortex reflects planetary waves decreasing deceleration and preserving axial symmetry of the flow. Stenchikov et al. [8] also found that tropospheric cooling caused by volcanic aerosols can affect storminess and generation of planetary waves in the troposphere. This tends to decrease

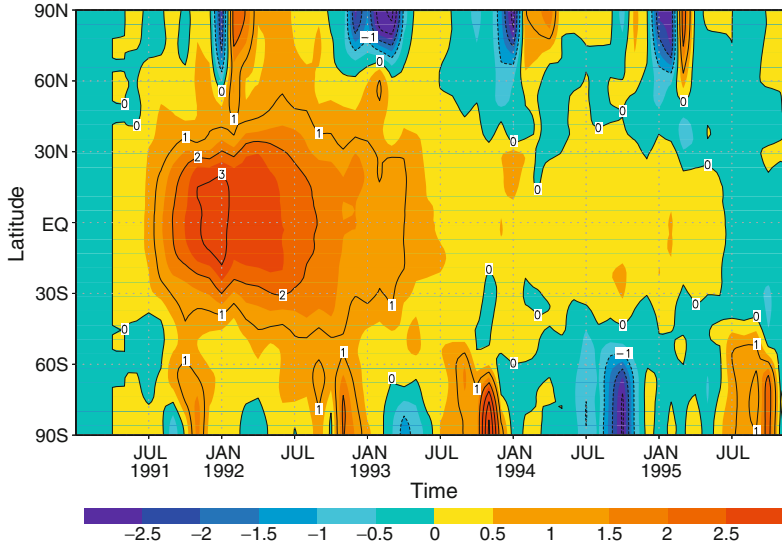

FIGURE 6 Zonal and ensemble mean stratospheric temperature anomaly (K) at 50 hPa (at about 25 km) calculated with respect to control experiment.

the flux of wave activity and negative angular momentum from the troposphere into the polar stratosphere, reducing wave drag on the vortex. To show this, Stenchikov et al. [8] conducted experiments with only solar, mostly tropospheric and surface cooling (no stratospheric warming). In these experiments, a positive phase of the AO was also produced because aerosol-induced tropospheric cooling in the subtropics decreases the meridional temperature gradient in the winter troposphere between 30°N and 60°N. The corresponding reduction of mean zonal energy and amplitudes of planetary waves in the troposphere decreases wave activity flux into the lower stratosphere. The resulting strengthening of the polar vortex forces a positive phase of the AO.

The high-latitude eruptions cannot warm lower stratosphere, and cannot cool subtropics as much as can low-latitude eruptions. Oman et al. [74] used GISS Model-E to simulate a climate impact of the 1912 Katmai eruption in Alaska. They calculated a 20-member ensemble of simulations and found that the volcanic aerosol cloud spread mostly north of 30 N could not produce a significant winter warming pattern even if it produced a higher hemispheric optical depth than that of the Pinatubo eruption in 1991.

Stenchikov et al. [8] also partitioned the dynamic effect of polar stratospheric ozone loss, caused by heterogeneous chemistry initiated by volcanic aerosols in the post-Pinatubo period. They found that ozone depletion caused a positive phase of the AO in late winter and early spring by cooling the lower

stratosphere in high latitudes, strengthening the polar night jet and delaying the final warming.

With respect to the dynamical mechanisms through which perturbations of the stratospheric annular circulation can influence tropospheric annular modes, Song and Robinson [82] pointed out that tropospheric westerlies can be strengthened by changes of planetary wave vertical propagation and/or reflection within the stratosphere and associated wave–zonal flow interaction [77,81,83], downward control or the nonlinear effect of baroclinic eddies [84–87]. All these mechanisms could play a role in shaping tropospheric dynamic response to volcanic forcing. The diagram in Fig. 7 schematically shows the processes involved in the AO/NAO sensitivity to volcanic forcing.

The up-to-date climate models formally include all those processes shown in Fig. 7 but can not produce the observed amplitude of the AO/NAO variability [39,75]. Shindell et al. [6] reported that the General Circulation Model (GCM) has to well resolve processes in the middle atmosphere in order to reproduce stratospheric influence to the troposphere. Stenchikov et al. [39] composited responses from nine volcanic eruptions using observations and IPCC AR4 model runs. They showed that all models produce a stronger polar vortex in the Northern Hemisphere as a response to volcanic forcing but the dynamic signal penetrated to the troposphere is much weaker in the models than in observations. Figure 8 shows simulations by different models in the

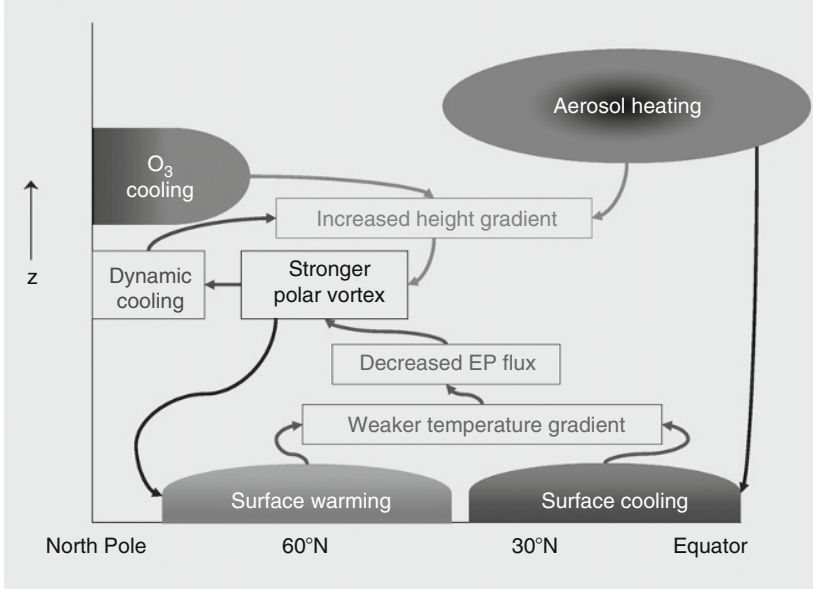

FIGURE 7 Schematic diagram depicting how the stratospheric and tropospheric gradient mechanisms are triggered by volcanic aerosol clouds in the tropical stratosphere. The wave feedback mechanism amplifies the response.

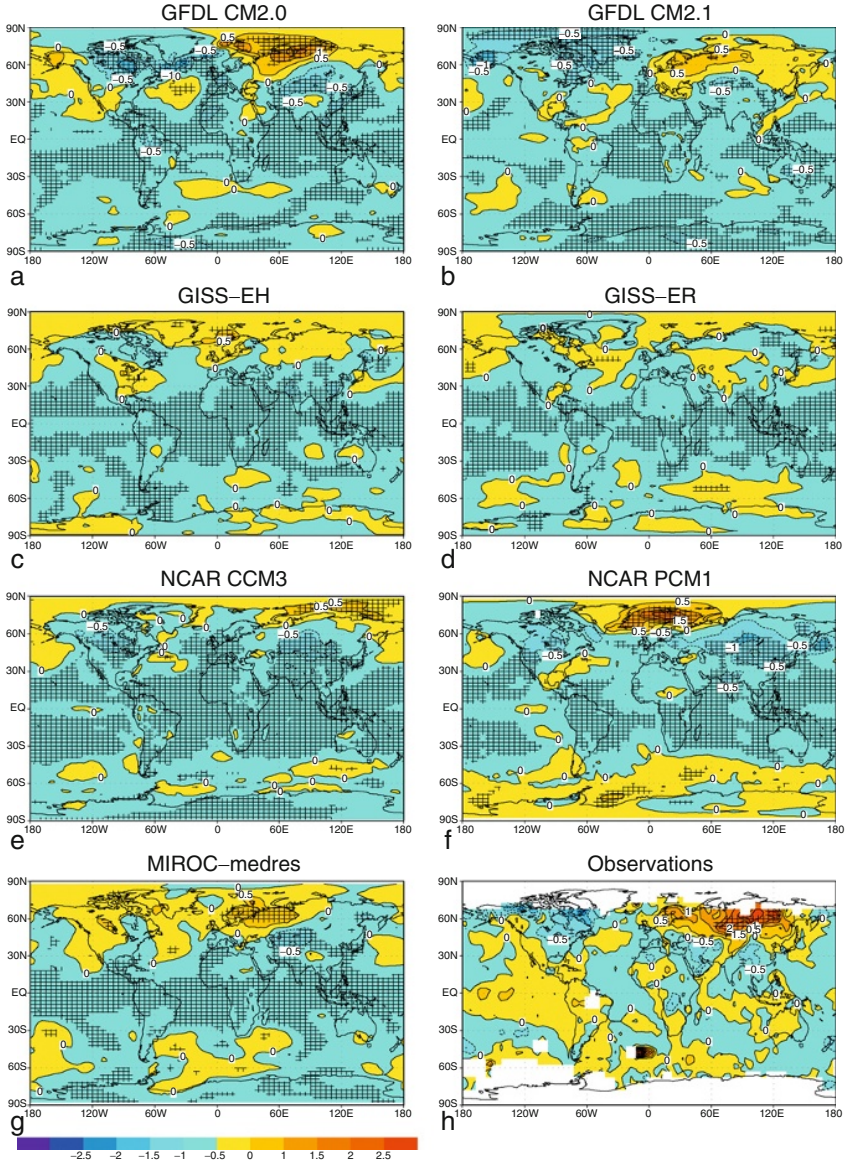

FIGURE 8 Surface winter (DJF) air temperature anomalies (K) composited for nine major volcanic eruptions from 1883 until present and averaged for two seasons and all available ensemble members: IPCC AR4 model simulations (a–g); observations from HadCRUT2v dataset (h). Hatching shows the areas with at least 90% confidence level calculated using a two-tailed local *t*-test.

course of the IPCC AR4 study, and observed winter warming from Stenchikov et al. [39] that caused by a pole-ward shift of tropospheric jet and more intensive transport of heat from ocean to land. The model tends to produce winter warming but significantly underestimates it.

It should be mentioned that the dynamic response to volcanic forcing could interact with the QBO that modulates the strength of polar vortex: it weakens and destabilizes the polar vortex in its easterly phase and makes it stronger and more stable in its westerly phase. The Mt. Pinatubo eruption of 1991 again provides a unique opportunity to test this interaction because in the winter of 1991/92 the QBO was in its easterly phase and in the winter of 1992/93 in its westerly phase. Stenchikov et al. [7] developed a version of the SKYHI troposphere–stratosphere–mesosphere model that effectively assimilates observed zonal mean winds in the tropical stratosphere to simulate a very realistic QBO and performed an ensemble of 24 simulations for the period 1 June 1991 to 31 May 1993. The model produced a reasonably realistic representation of the positive AO response in boreal winter that is usually observed after major eruptions. Detailed analysis shows that the aerosol perturbations to the tropospheric winter circulation are affected significantly by the phase of the QBO, with a westerly QBO phase in the lower stratosphere resulting in an enhancement of the aerosol effect on the AO. Improved quantification of the QBO effect on climate sensitivity helps to better understand mechanisms of the stratospheric contribution to natural and externally forced climate variability.

3.4. Volcanic Impact on Ocean Heat Content and Sea Level

The Earth's oceans comprise almost the entire thermal capacity of the climate system. Their thermal inertia delays full-scale response of the Earth's surface temperature to greenhouse warming [88]. The rate at which heat accumulates in oceans is an important characteristic of global warming. It is a complex process that involves slow energy diffusion and large-scale transport in MOC, as well as faster vertical mixing by seasonal thermo-haline convection and by wind-driven gyres.

Observations and model simulations show that the ocean warming effect of the relatively steadily developing anthropogenic forcings is offset by the sporadic cooling caused by major explosive volcanic eruptions [43,45,46]. Delworth et al. [44] conducted a series of historic runs from 1860 to 2000 in the framework of the IPCC AR4 study using GFDL CM2.1, and partitioning contributions of different forcings. Figure 9 shows the ensemble mean ocean heat content anomalies in the 0–3000 m depth range for a subset of the runs from Delworth et al. [44], calculated accounting for all the time varying forcing agents ('ALL') and for volcanic and solar forcings only ('NATURAL'). However, the solar effect for this period is small compared to the volcanic effect. The 'ALL' compares well with the Levitus et al. [89]

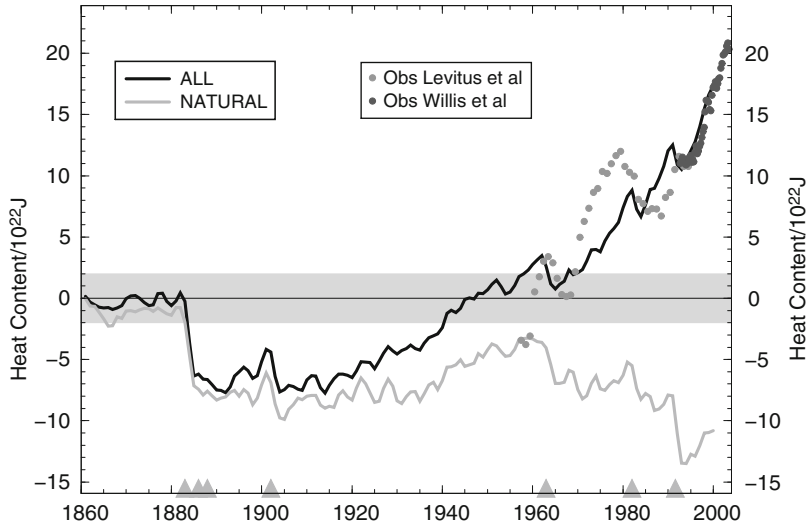

FIGURE 9 The ensemble mean ocean heat content anomalies in the 0–3000 m ocean layer. 'ALL' refers to the ensemble mean calculated with all the time varying forcing agents: well mixed greenhouse gases, anthropogenic aerosols, stratospheric and tropospheric ozone, land use, solar irradiance and volcanic aerosols. 'NATURAL' refers to the ensemble calculated accounting for volcanic and solar forcings only. The red and purple circles depict observational estimates based on, respectively, over 0–3000 m layer [89] and over 0–750 m layer [90]. Constant offsets have been added to the observed data so that their means were the same as the model data over the period of overlap. The shaded triangles along the time-axes denote the times of major volcanic eruptions. The shading shows plus or minus 2-standard deviations of ocean heat content estimated from a 2000 a control run of the climate model with forcings fixed at the 1860 level.

and Willis et al. [90] observations shown in Fig. 9, and, even better, with the improved analyses from Carton et al. [91] and Dominigues et al. [92] (not shown). Both 'ALL' and 'NATURAL' anomalies are highly statistically significant and far exceed the 'CONTROL' variability shown by shading. The cumulative cooling effect of natural forcings reaches 10^{23} J by year 2000, which is right between the estimates obtained by Church et al. [43] and Gleckler et al. [45] who conducted similar analysis, and offsets about one third of 'ALL' minus 'NATURAL' ocean warming. The volcanic signal exceeds two standard deviations of unforced variability throughout the entire run since the Krakatau eruption in 1883. This result suggests that the observed frequency and strength of the Earth's explosive volcanism in the nineteenth and twentieth centuries [1] was sufficient to produce a 'quasi-permanent' signature in the global oceans. Also, ocean warming (cooling) causes expansion (contraction) of water and therefore affects sea level or, so called, thermosteric height. This effect comprises a significant portion of the observed contemporary sea level rise.

To better quantify volcanic impact on ocean, Stenchikov et al. [47] calculated a 10-member ensemble of volcano and control 20-year experiments for the Pinatubo period 1991–2010. They found that in contrast to the atmospheric temperature responses the ocean heat content and the steric height remain well above noise level for decades. Figures 10 and 11 show anomalies of the global ocean heat content and the steric height for the Pinatubo ensembles calculated for the whole-depth ocean and for the upper 300 m layer. The ocean integrates the surface radiative cooling from the volcanic eruption. Since the volcanic aerosols and associated cooling persist for about 3 years, the anomalies in Figs. 10 and 11 reach their maximum value after about this time when the volcanic radiative forcing vanishes. The maximum heat content and sea level decrease in our Pinatubo simulation is 5×10^{22} J and 9 mm, respectively.

The characteristic time, defined as e-folding time for ocean heat content or steric height, is about 40–50 a. Assuming that the complete relaxation requires two to three relaxation times, this might take more than a century, and that length of time is sufficiently long for another strong eruption to happen. Therefore, the 'volcanic' cold anomaly in the ocean never disappears at the present frequency of the Earth's explosive volcanism.

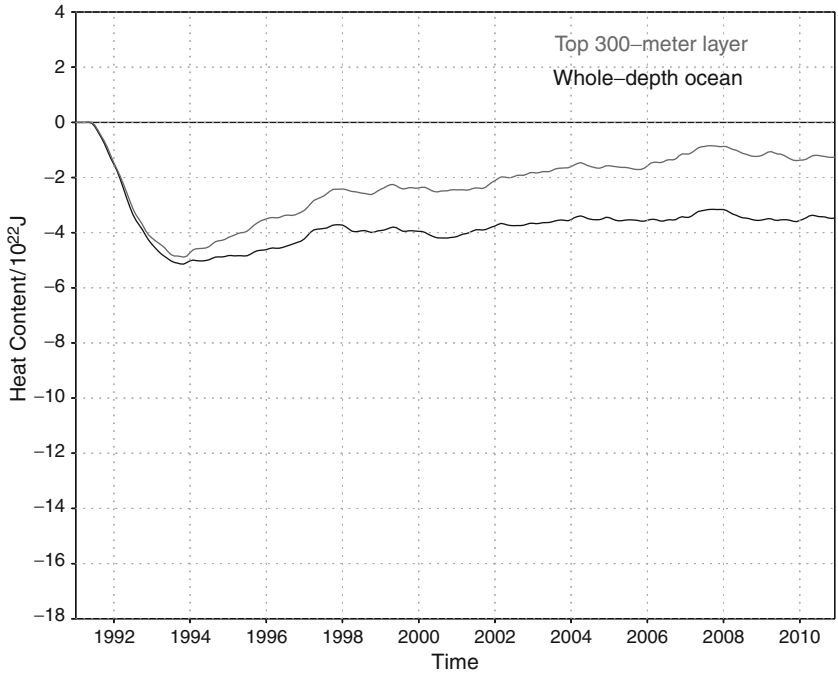

FIGURE 10 The global and ensemble mean ocean heat content (10^{22} J) anomaly for 300-m and whole depth ocean for the Pinatubo ensemble calculated with respect to ensemble control.

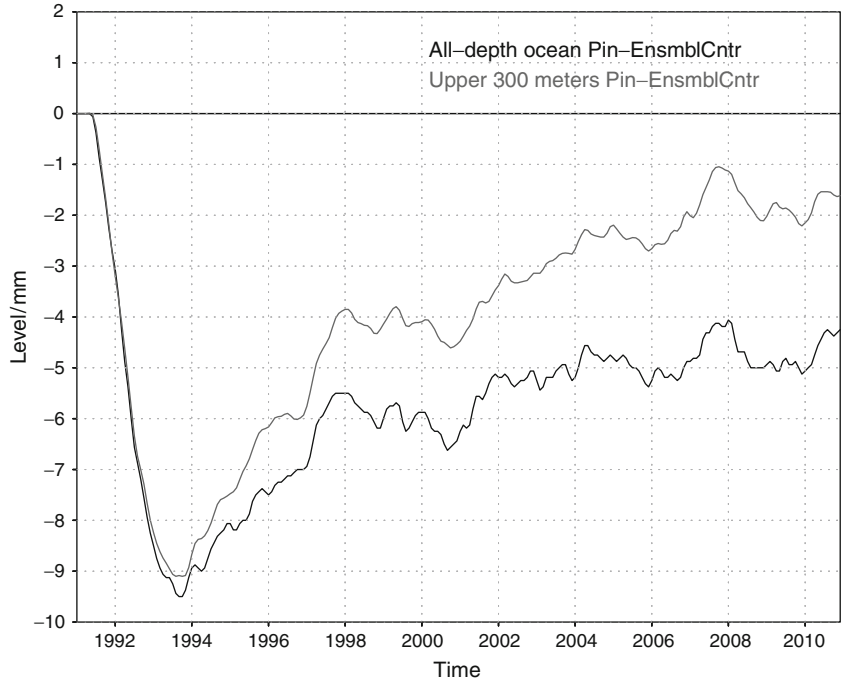

FIGURE 11 The global and ensemble mean thermosteric height anomalies (mm) for 300-m and whole depth ocean for the Pinatubo ensemble calculated with respect to ensemble control.

3.5. Strengthening of Overturning Circulation

The short-wave cooling from volcanic aerosol results in a cold surface temperature anomaly that develops during the first 3 years until volcanic aerosols vanish. Cold surface water is gradually transferred into the deeper ocean layers. A volcanically induced cooling leads to reduced precipitation and river runoff at high latitudes of the Northern Hemisphere, thereby leading to more saline (and hence denser) upper ocean conditions in the higher latitudes of the Northern Hemisphere. Both these factors (colder ocean temperature and enhanced salinity) destabilise the water column, making them more prone to ocean convection. The increased ocean convection tends to enhance the MOC. Further, an enhanced positive phase of the AO also leads to an MOC increase [93].

As a result, the MOC increases in response to the volcanic forcing (see Fig. 12). The maximum increase is 1.8 Sverdrups or about 9% (Sv; 1 Sv = 10^6 $m^3 \cdot s^{-1}$). The MOC has inherent decadal time scales of adjustment, and is thus maximum at some 5–15 a after the volcanic eruptions. An increase in

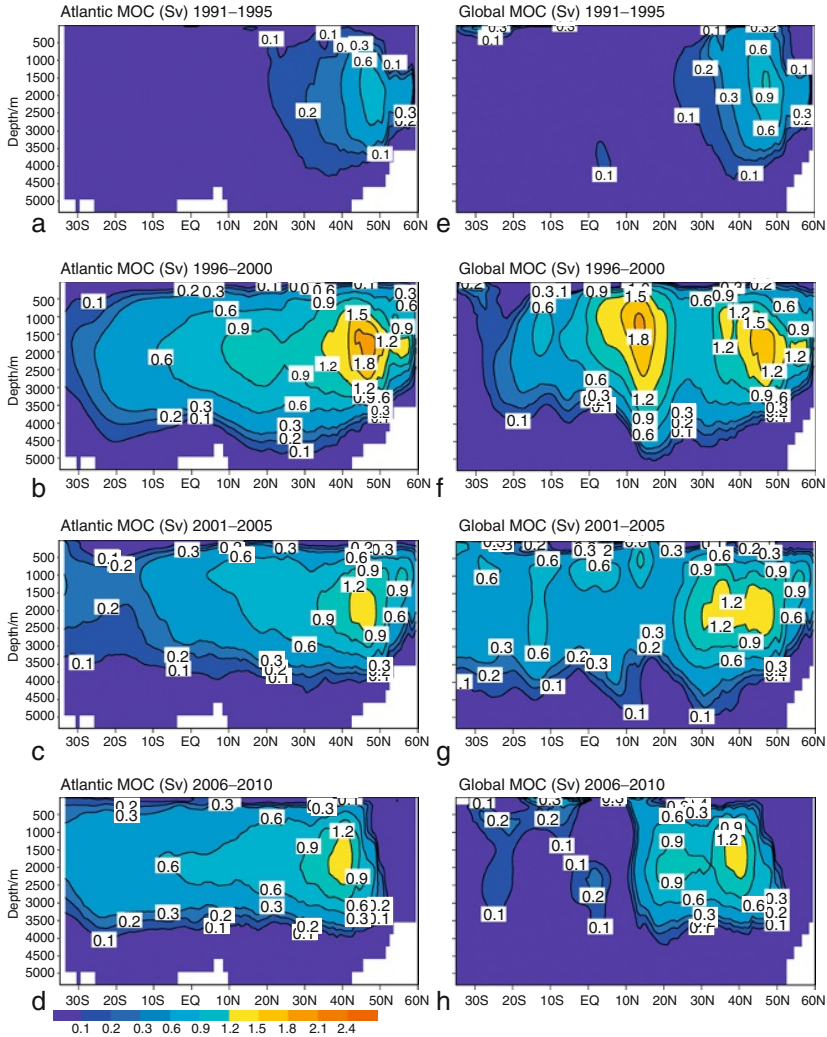

FIGURE 12 The 5-year means MOC anomalies (Sv) from the Pinatubo ensemble averaged zonally over Atlantic basin (a–d) and over the globe (e–h).

MOC also could cause in part the asymmetry of the ocean temperature response in the high northern and southern latitudes.

The simulations show a tendency for cooling of the deep waters in the Southern Ocean and warming in the deep waters of the Northern Ocean. This asymmetry could also be caused in part by the redistribution of ocean salinity, the forced positive phase of the AO during a few years following a volcanic eruption, and by a significant increase of sea ice extent and volume in the Northern Hemisphere.

3.6. Volcanic Impact on Sea Ice

The effect of volcanic forcing on the sea ice extent in the Northern Hemisphere is of great interest because significant loss of perennial sea ice under global warming is occurring in the Northern Hemisphere. Therefore, it is very important to better understand what factors could affect them the most. Figures 13 and 14 show the anomaly of the northern hemispheric mean annual maximum and minimum ice extent and mass for the Pinatubo runs. The Maximum Sea Ice Extent anomalies reach 0.6×10^6 km^2 in the Pinatubo run – it takes at least 5 years to develop. So, sea ice extent responds more strongly not to the radiative forcing but to ocean temperature and circulation. The sea ice extent relaxes to zero for a decade. It must be mentioned that both observed and simulated ice extent anomalies are not statistically significant, though in simulations they exceed one standard deviation. The minimum ice extent is more sensitive to radiative cooling and ocean temperature; therefore, its anomaly is stronger than the anomaly of the maximum ice extent reaching 0.9×10^6 km^2. It builds up in 3 years when the strongest ocean cooling develops and then declines for about 10 years.

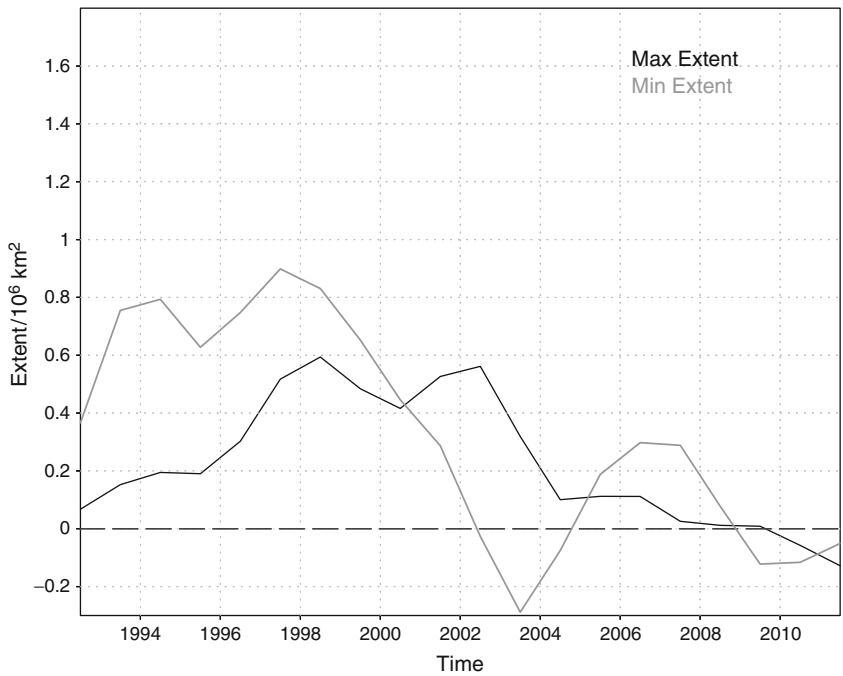

FIGURE 13 The Northern Hemisphere anomalies of maximum and minimum ice extent (10^6 km^2) for the Pinatubo ensemble.

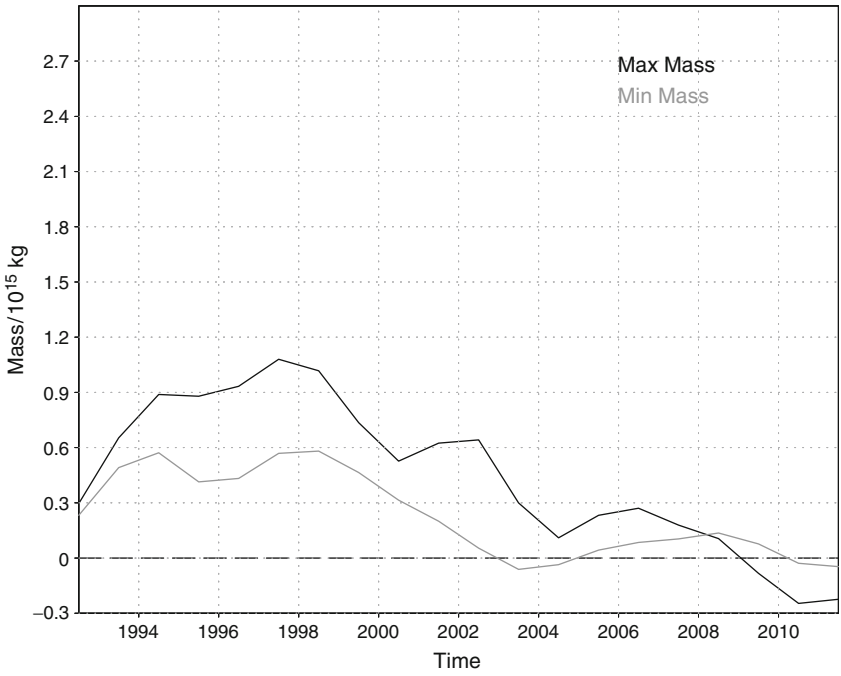

FIGURE 14 The Northern Hemisphere anomalies of maximum and minimum ice mass (10^{15} kg) for the Pinatubo ensemble.

4. SUMMARY

Volcanic eruptions force all elements of the climate system, producing long-term climate signals in ocean. The cumulative volcanic cooling effect at present offsets about one third of anthropogenic ocean warming [44]. In the atmosphere, however, volcanic signals are masked by meteorological noise in about 7 years in the model ensembles and much sooner in the real world. Radiative forcing produced by explosive volcanic events that have occurred in historic periods lasts for about 3 years. The volcanically induced tropospheric temperature anomalies reduce below noise for ~7 years. The sea ice responds on the decadal time scale. Deep ocean temperature, sea level, salinity and MOC have relaxation times of several decades to a century. Volcanic eruptions produce long-term impacts on the ocean's subsurface temperature and steric height that accumulate at the current frequency of explosive volcanic events. The vertical distribution of the ocean temperature change signal is asymmetric at high latitudes. A cooling signal penetrates to depth at high Southern latitudes, while a warming signal penetrates to depth at high latitudes of the Northern Hemisphere. This asymmetry is caused in part by an

increase in MOC. The decrease of ocean steric height in our simulations, caused by the Pinatubo eruption, reaches 9 mm in comparison with 5 mm estimated by Church et al. [43] from observations. The ocean heat content decreases by 5×10^{22} J. The maximum sea ice extent and ice mass increase in the Pinatubo runs by 0.5×10^6 km^2 and 1.0×10^{15} kg, respectively. This corresponds to 3% and 5% of the model 'control' maximum extent and mass in the Pinatubo runs. The simulated minimum ice extent is more sensitive to volcanic forcing than the maximum ice extent. The Atlantic MOC strengthens in the Pinatubo runs very significantly by 1.8 Sv or 9% of its maximum value.

Atmospheric temperature anomalies forced by the Pinatubo eruption in the troposphere and lower stratosphere are well reproduced by the models. However, forced AO/NAO responses are underestimated and observed sea level and ocean heat content anomalies are overestimated by all models. Nevertheless, all model results and observations suggest that volcanoes could produce long-lasting impact on ocean heat content and thermo-steric level that, in fact, could affect estimates of current climate trends. Quasi-periodic nature of volcanic cooling facilitates ocean vertical mixing and might have an important effect on the thermal structure of the deep ocean. Therefore, it has to be realistically implemented in climate models for calculating 'quasi-equilibrium' initial conditions, climate reconstructions and for future climate projections.

ACKNOWLEDGEMENTS

This work was supported in part by NASA grant NNG05GB06G, NSF grantATM-0351280, by UCAR Visiting Scientist Program and by the NOAA Geophysical Fluid Dynamics Laboratory (GFDL).

REFERENCES

1. T. Simkin, Annu. Rev. Earth Planet Sci. 21 (1993) 427–452.
2. G.L. Stenchikov, I. Kirchner, A. Robock, H.F. Graf, J.C. Antuña, R.G. Grainger, A. Lambert, L. Thomason, J. Geophys. Res. 103 (1998) 13837–13857.
3. M. Collins, in: A. Robock, C. Oppenheimer (Eds.), Predictions of Climate Following Volcanic Eruptions, American Geophysical Union, Washington, DC, 2003, pp. 283–300.
4. D. Shindell, G. Schmidt, M. Mann, G. Faluvegi, J. Geophys. Res. 109 (2004) D05104.
5. D. Shindell, G. Schmidt, R. Miller, M. Mann, J. Clim. 16 (2003) 4094–4107.
6. D.T. Shindell, G.A. Schmidt, R.L. Miller, D. Rind, J. Geophys. Res. 106 (2001) 7193–7210.
7. G. Stenchikov, K. Hamilton, A. Robock, V. Ramaswamy, M.D. Schwarzkopf, J. Geophys. Res. 109 (2004) D03112.
8. G. Stenchikov, A. Robock, V. Ramaswamy, M.D. Schwarzkopf, K. Hamilton, S. Ramachandran, J. Geophys. Res. 107 (2002) 4803.
9. G.J. Boer, M. Stowasser, K. Hamilton, Clim. Dyn. 28 (2007) 481–502.
10. B.J. Soden, R.T. Wetherald, G.L. Stenchikov, A. Robock, Science 296 (2002) 727–730.
11. T.M.L. Wigley, C.M. Ammann, B.D. Santer, S.C.B. Raper, J. Geophys. Res. 110 (2005) D09107.

12. M.L. Asaturov, M.I. Budyko, K.Y. Vinnikov, P.Y. Groisman, A.S. Kabanov, I.L. Karol, M.P. Kolomeev, Z.I. Pivovarova, E.V. Rozanov, S.S. Khmelevtsov, Volcanic Stratospheric Aerosols and Climate (in Russian), St. Petersburg, Russia, Gidrometeoizdat, 1986, 256pp.
13. H.W. Elsaesser, Isolating the climatologic effects of volcanoes. Report UCRL-89161. Lawrence Livermore National Laboratory, Livermore, CA, 1983, 29pp.
14. K.Y. Kondratyev, Volcanoes and Climate. WCP-54, WMO/TD-166, World Meteorological Organisation, Geneva, 1988, 103pp.
15. K.Y. Kondratyev, I. Galindo, Volcanic Activity and Climate, A. Deepak, Hampton, VA, 1997, 382pp.
16. H.H. Lamb, Philos. Trans. R. Soc. Lond. Ser. A 266 (1970) 425–533.
17. A. Robock, Rev. Geophys. 38 (2000) 191–219.
18. O.B. Toon, in: A. Deepak (Ed.), Atmospheric Effects and Potential Climatic Impact of the 1980 Eruptions of Mount St. Helems, NASA Conference Publication 2240, 1982, pp. 15–36.
19. O.B. Toon, J.B. Pollack, Am. Sci. 68 (1980) 268–278.
20. M.F. Gerstell, J. Crisp, D. Crisp, J. Clim. 8 (1995) 1060–1070.
21. D.J. Lary, M. Balluch, S. Bekki, Q J R Meteorol. Soc. 120 (1994) 1683–1688.
22. W. Zhong, J. Haigh, R. Toumi and S. Bekki, Q. J. R. Meteorol. Soc. 122 (1996) 1459–1466.
23. D. Budner, J. Cole-Dai, in: A. Robock, C. Oppenheimer (Eds.), The Number and Magnitudes of Large Explosive Volcanic Eruptions Between 904 and 1865 A.D.: Quanitative Evidence From A New South Pole Ice Core, American Geophysical Union, Washington, DC, 2003, pp. 165–176.
24. E. Mosley-Thompson, T.A. Mashiotta, L.G. Thompson, in: A. Robock, C. Oppenheimer (Eds.), High Resolution Ice Core Records of Late Holocene Volcanism: Current and Future Contributions From The Greenland PARCA Cores, American Geophysical Union, Washington, DC, 2003, pp. 153–164.
25. K. Yalcin, C. Wake, M. Germani, J. Geophys. Res. 107 (2002) 4012.
26. A.J. Krueger, S.J. Schaefer, N.A. Krotkov, G. Bluth, S. Barker, Geophys. Monograph 116 (2000) 25–43.
27. A. Prata, W. Rose, S. Self, D. O'Brien, in: A. Robock, C. Oppenheimer (Eds.), Global, Long-Term Sulphur Dioxide Measurements From TOVS Data: A New Tool For Studying Explosive Volcanism and Climate, American Geophysical Union, Washington, DC, 2003, pp. 75–92.
28. J.C. Antuña, A. Robock, G.L. Stenchikov, L.W. Thomason, J.E. Barnes, J. Geophys. Res.-Atm. 107 (2002) pp. 4194.
29. J.C. Antuña, A. Robock, G.L. Stenchikov, J. Zhou, C. David, J. Barnes, L. Thomason, J. Geophys. Res. 108 (2003) 4624.
30. C.E. Randall, R.M. Bevilacqua, J.D. Lumpe, K.W. Hoppel, J. Geophys. Res. 106 (2001) 27525–27536.
31. C.E. Randall, R.M. Bevilacqua, J.D. Lumpe, K.W. Hoppel, D.W. Rusch, E.P. Shettle, J. Geophys. Res. 105 (2000) 3929–3942.
32. L. Thomason, T. Peter, Assessment of Stratospheric Aerosol Properties. WCRP-124, WMO/TD-1295, SPARC Report 4. World Climate Research Program. (2006) 318pp.
33. L.W. Thomason, G. Taha, Geophys. Res. Lett. 30 (2003) 1631.
34. C. Amman, G. Meehl, W. Washington, C. Zender, Geophys. Res. Lett. 30 (2003) 1657.
35. J. Bauman, P. Russell, M. Geller, P. Hamill, J. Geophys. Res. 108 (2003) 4382.
36. J. Bauman, P. Russell, M. Geller, P. Hamill, J. Geophys. Res. 108 (2003) 4383.
37. J. Hansen, J. Geophys. Res. 107 (2002) 4347.
38. M. Sato, J. Hansen, M.P. McCormick, J. Pollack, J. Geophys. Res. 98 (1993) 22987–22994.

39. G. Stenchikov, K. Hamilton, R.J. Stouffer, A. Robock, V. Ramaswamy, B. Santer, H.F. Graf, J. Geophys. Res. 111 (2006) D07107.
40. C. Bingen, D. Fussen, F. Vanhellemont, J. Geophys. Res. 109 (2004) D06201.
41. C. Bingen, D. Fussen, F. Vanhellemont, J. Geophys. Res. 109 (2004) D06202.
42. A. Robertson, J. Overpeck, D. Rind, E. Mosley-Thomson, G. Zelinski, J. Lean, D. Koch, J. Penner, I. Tegen, R. Healy, J. Geophys. Res. 106 (2001) 14783–14803.
43. J. Church, N. White, J. Arblaster, Nature 438 (2005) 74–77.
44. T.L. Delworth, V. Ramaswamy, G.L. Stenchikov, Geophys. Res. Lett. 32 (2005) L24709.
45. P.J. Gleckler, T.M.L. Wigley, B.D. Santer, J.M. Gregory, K. AchutaRao, K.E. Taylor, Nature 439 (2006) 675.
46. J. Gregory, J. Lowe, S. Tett, J. Clim. 19 (2006) 4576–4591.
47. G. Stenchikov, V. Ramaswamy, T. Delworth, Impact of Big Tambora Eruption on ENSO, Ocean Heat Uptake, and Sea Level, PP31E-07, Presented at 2007 Fall AGU Meeting, San Francisco, CA, 2007.
48. A.J. Baran, J.S. Foot, J. Geophys. Res. 99 (1994) 25673–25679.
49. J.E. Barnes, D.J. Hoffman, Geophys. Res. Lett. 24 (1997) 1923–1926.
50. G.J.S. Bluth, S.D. Doiron, A.J. Krueger, L.S. Walter, C.C. Schnetzler, Geophys. Res. Lett. 19 (1992) 151–154.
51. G.J.S. Bluth, W.I. Rose, I.E. Sprod, A.J. Krueger, J. Geol. 105 (1997) 671–683.
52. A. Lambert, R.G. Grainger, J.J. Remedios, C.D. Rogers, M. Corney, F.W. Taylor, Geophys. Res. Lett. 20 (1993) 1287–1290.
53. W.G. Read, L. Froidevaux, J.W. Waters, Geophys. Res. Lett. 20 (1993) 1299–1302.
54. P. Minnis, E.F. Harrison, L.L. Stowe, G.G. Gibson, F.M. Denn, D.R. Doelling, W.L. Smith Jr., Science 259 (1993) 1411–1415.
55. T. Crowley, Science 289 (2000) 270–277.
56. A. Broccoli, K. Dixon, T. Delworth, T. Knutson, R. Stouffer, J. Geophys. Res. 108 (2003) 4798.
57. GFDL. CM2.x References, 2006, Available from: http://nomads.gfdl.noaa.gov/CM2.X/references.
58. S.-J. Lin, Monthly Weather Rev. 132 (2004) 2293–2307.
59. P.C.D. Milly, A.B. Shmakin, J. Hydrometeor. 3 (2002) 283–299.
60. A. Gnanadesikan, K.W. Dixon, S.M. Griffies, V. Balaji, M. Barreiro, J.A. Beesley, W.F. Cooke, T.L. Delworth, R. Gerdes, M.J. Harrison, I.M. Held, W.J. Hurlin, H.-C. Lee, Z. Liang, G. Nong, R.C. Pacanowski, A. Rosati, J. Russell, B.L. Samuels, Q. Song, M.J. Spelman, R.J. Stouffer, C.O. Sweeney, G. Vecchi, M. Winton, A.T. Wittenberg, F. Zeng, R. Zhang, J.P. Dunne, J. Clim. 19 (2006) 675–697.
61. S.M. Griffies, A. Gnanadesikan, K.W. Dixon, J.P. Dunne, R. Gerdes, M.J. Harrison, A. Rosati, J.L. Russell, B.L. Samuels, M.J. Spelman, M. Winton, R. Zhang, Ocean Sci. 1 (2005) 45–79.
62. M. Winton, J. Atmos. Oceanic Technol. 17 (2000) 525–531.
63. J.B. Adams, M.E. Mann, C.M. Ammann, Nature 426 (2003) 274–278.
64. B.D. Santer, T.M.L. Wigley, C. Doutriaux, J.S. Boyle, J.E. Hansen, P.D. Jones, G.A. Meehl, E. Roeckner, S. Sengupta, K.E. Taylor, J. Geophys. Res. 106 (2001) 28033–28059.
65. F. Yang, M. Schlesinger, J. Geophys. Res. 106 (2001) 14757–14770.
66. F. Yang, M. Schlesinger, J. Geophys. Res. 107 (2002) 4073.
67. J.R. Christy, R.W. Spencer, W.D. Braswell, J. Atmos. Oceanic Technol. 17 (2000) 1153–1170.
68. S. Manabe, R.J. Stouffer, J. Geophys. Res. 85 (1980) 5529–5554.

69. I. Kirchner, G. Stenchikov, H. Graf, A. Robock, J. Antuña, J. Geophys. Res. 104 (1999) 19039–19055.
70. V. Ramaswamy, M.D. Schwarzkopf, W. Randel, B. Santer, B.J. Soden, G. Stenchikov, Science 311 (2006) 1138–1141.
71. K. Trenberth, A. Dai, Geophys. Res. Lett. 34 (2007) L15702.
72. L. Oman, A. Robock, G.L. Stenchikov, T. Thordarson, Geophys. Res. Lett. 33 (2006) L18711.
73. A. Robock, Y. Liu, J. Clim. 7 (1994) 44–55.
74. L. Oman, A. Robock, G. Stenchikov, G.A. Schmidt, R. Ruedy, J. Geophys. Res. 110 (2005) D13103.
75. R.L. Miller, G.A. Schmidt, D. Shindell, J. Geophys. Res. 111 (2006) D18101.
76. A. Robock, T. Adams, M. Moore, L. Oman, G. Stenchikov, Geophys. Res. Lett. 34 (2007) L23710.
77. K. Kodera, J. Geophys. Res. 99 (1994) 1273–1282.
78. K. Kodera, Y. Kuroda, Geophys. Res. Lett. 27 (2000) 3349–3352.
79. K. Kodera, Y. Kuroda, J. Geophys. Res. 105 (2000) 12361–12370.
80. Y. Ohhashi, K. Yamazaki, J. Meteorol. Soc. Jpn. 77 (1999) 495–511.
81. J. Perlwitz, H.-F. Graf, J. Clim. 8 (1995) 2281–2295.
82. Y. Song, W.A. Robinson, J. Atmos. Sci. 61 (2004) 1711–1725.
83. J. Perlwitz, N. Harnik, J. Clim. 16 (2003) 3011–3026.
84. R. Black, J. Clim. 15 (2002) 268–277.
85. R.X. Black, B.A. McDaniel, J. Clim. 17 (2004) 3990–4004.
86. P.H. Haynes, M.E. McIntyre, T.G. Shepherd, C.J. Marks, K.P. Shine, J. Atmos. Sci. 48 (1991) 651–680.
87. V. Limpasuvan, D.J.W. Thompson, D.L. Hartmann, J. Clim. 17 (2004) 2584–2596.
88. G. Meehl, W. Washington, W. Collins, J. Arblaster, A. Hu, L. Buja, W. Strand, H. Teng, Science 307 (2005) 1769–1772.
89. S. Levitus, J. Antonov, T. Boyer, Geophys. Res. Lett. 32 (2005) L02604.
90. J.K. Willis, D. Roemmich, B. Cornuelle, J. Geophys. Res. 109 (2004) C12036.
91. J. Carton, A. Santorelli, J. Clim. 2008, 21 (22), 6015–6035.
92. C. Dominigues, J. Church, N. White, P. Gleckler, S. Wijffels, P. Barker, J. Dunn, Nature 453 (2008) 1090–1093.
93. T.L. Delworth, K.W. Dixon, Geophys. Res. Lett. 33 (2006) L02606.